Inversion doublets of reflection-asymmetric clustering in ^{28}Si and their isoscalar monopole and dipole transitions

Y. Chiba
Department of Physics, Hokkaido University, Sapporo 060-0810, Japan

Y. Taniguchi
Department of Information Engineering, National Institute of Technology, Kagawa college, Takamatsu 761-8058, Japan

M. Kimura
Department of Physics, Hokkaido University, Sapporo 060-0810, Japan
and Nuclear Reaction Data Centre, Faculty of Science, Hokkaido University, Sapporo 060-0810, Japan

(Received 13 October 2016; published 28 April 2017)

Background: Various cluster states of astrophysical interest are expected to exist in the excited states of ^{28}Si. However, they have not been identified firmly, because of the experimental and theoretical difficulties.
Purpose: To establish the $^{24}\mathrm{Mg}+\alpha$, $^{16}\mathrm{O}+^{12}\mathrm{C}$, and $^{20}\mathrm{Ne}+2\alpha$ cluster bands, we theoretically search for the negative-parity cluster bands that are paired with the positive-parity bands to constitute the inversion doublets. We also offer the isoscalar monopole and dipole transitions as a promising probe for the clustering. We numerically show that these transition strengths from the ground state to the cluster states are very much enhanced.
Method: The antisymmetrized molecular dynamics with Gogny D1S effective interaction is employed to calculate the excited states of ^{28}Si. The isoscalar monopole and dipole transition strengths are directly evaluated from wave functions of the ground and excited states.
Results: Negative-parity bands having $^{24}\mathrm{Mg}+\alpha$ and $^{16}\mathrm{O}+^{12}\mathrm{C}$ cluster configurations are obtained in addition to the newly calculated $^{20}\mathrm{Ne}+2\alpha$ cluster bands. All of them are paired with the corresponding positive-parity bands to constitute the inversion doublets with various cluster configurations. The calculation shows that the bandheads of the $^{24}\mathrm{Mg}+\alpha$ and $^{20}\mathrm{Ne}+2\alpha$ cluster bands are strongly excited by the isoscalar monopole and dipole transitions.
Conclusions: The present calculation suggests the existence of inversion doublets with the $^{24}\mathrm{Mg}+\alpha$, $^{16}\mathrm{O}+^{12}\mathrm{C}$, and $^{20}\mathrm{Ne}+2\alpha$ configurations. Because of the enhanced transition strengths, we offer the isoscalar monopole and dipole transitions as good probe for the $^{24}\mathrm{Mg}+\alpha$ and $^{20}\mathrm{Ne}+2\alpha$ cluster bands.

DOI: 10.1103/PhysRevC.95.044328

I. INTRODUCTION

Compared to light p-shell nuclei where the α clustering is prominent in the ground and excited states [1], the structure of the sd-shell nuclei is more complicated and much richer. The formation of the mean field in the low-lying states and its coexistence and mixing with the α, carbon, and oxygen clustering yield various kinds of nuclear structures [2–4]. ^{28}Si is a typical example in the mid sd-shell nuclei. Its ground-state band has oblate deformed mean-field structure, while the rotational band built on the 0^+_3 state is prolately deformed, suggesting shape coexistence [5–8]. It is believed that the β vibration of the ground-state band yields another rotational band built on the 0^+_2 state [5,8]. Furthermore, the possible existence of the superdeformed (SD) state is predicted by theoretical studies [4,9–13] and the experimental candidates were observed [14–17].

In addition to these mean-field dynamics, ^{28}Si offers a rich variety of clustering. Many candidates of $^{24}\mathrm{Mg}+\alpha$ cluster states are observed at more than 10 MeV above the ground state [18–22]. The existence of the $^{12}\mathrm{C}+^{16}\mathrm{O}$ molecular resonance above $E_x \simeq 30$ MeV is also well known [23–28]. In addition to these highly excited cluster states, the possible clustering of the above-mentioned low-lying mean-field states has attracted much interests and has long been discussed [4,12,29–32]. For example, in an antisymmetrized molecular dynamics (AMD) study [4], it was pointed out that the ground-state band and SD band have large overlap with the $^{24}\mathrm{Mg}+\alpha$ cluster configurations, while the prolate band largely overlaps with the $^{12}\mathrm{C}+^{16}\mathrm{O}$ configuration. A similar point was also made using the algebraic cluster model [9,13,33,34]. It is also noted that the α and carbon cluster states at their decay thresholds are of astrophysical interest and importance, because they are closely related to and seriously affect to stellar processes such as the He and C burning. Thus, the clustering phenomena in ^{28}Si are rich in variety and have scientific importance.

Despite this strong interest and the continuous experimental and theoretical efforts, the clustering systematics in ^{28}Si is still ambiguous. Theoretically, the description of various kinds of cluster configurations within a single theoretical framework is not easy. In particular, the coexistence and mixing of mean-field and cluster configurations makes the theoretical description hard, although it enriches the clustering phenomena in ^{28}Si. Experimentally, the direct production of the cluster states by the transfer and radiative capture reactions is difficult, because of their small cross sections and very high level density. These difficulties prevent us from understanding and establish the clustering systematics in ^{28}Si.

To overcome these difficulties, we present the result of the AMD calculation to illustrate the clustering systematics and suggest the isoscalar (IS) monopole and dipole transitions as a promising probe for clustering. We focus on the following two points. The first is the negative-parity cluster bands and the identification of the inversion doublets. The previous AMD study [4] investigated the structure of the positive-parity bands, and found that three positive-parity bands—the ground-state, prolate deformed, and SD bands—have large overlap with the triaxial deformed $^{24}\mathrm{Mg}+\alpha$, the $^{16}\mathrm{O}+{}^{12}\mathrm{C}$, and the axially symmetric $^{24}\mathrm{Mg}+\alpha$ cluster configurations, respectively. If these bands really have clustering aspects, they must be accompanied by the negative-parity bands to constitute the inversion doublets, because of their reflection-asymmetric intrinsic configurations [35]. Therefore, the identification of the inversion doublet is rather essential to establish the clustering systematics in ^{28}Si, and in this study we extend our survey to the negative-party states.

The second point is the IS monopole and dipole transitions, which are expected to strongly populate the cluster inversion doublets. In this decade, the IS monopole transition has attracted much interest as a good probe for the 0^+ cluster states [36–41]. In addition to this, recently it was also suggested that the IS dipole transition is a good probe for the 1^- cluster states [42]. Therefore, the combination of the IS monopole and dipole transitions is expected to be a powerful tool to identify the inversion doublets mentioned above. Indeed, in Refs. [39,42], by assuming that the ground states is a pure SU(3) shell model state [43,44] and the excited states are ideal cluster states, it was analytically proved that the IS monopole and dipole transitions from the ground state to the excited cluster states are as strong as the single-particle estimates. However, in reality, the ground state of ^{28}Si deviates from a pure SU(3) shell model state because of the strong influence of the spin-orbit interaction. Furthermore, in the excited states, the cluster configurations are mixed with the mean-field configurations. Therefore, the numerical calculations using the reliable nuclear models are indispensable for quantitative discussions.

In this paper, we show that the various kinds of cluster bands, including the newly found $^{20}\mathrm{Ne}+{}^{8}\mathrm{Be}$ band, appear in the negative-parity bands and pair with the positive-parity bands to constitute the inversion doublets. The analysis of the wave function shows that the ground state has the duality of an oblate deformed mean field and the clustering of $^{24}\mathrm{Mg}+\alpha$ and $^{20}\mathrm{Ne}+{}^{8}\mathrm{Be}$ despite the strong influence of the spin-orbit interaction. Because of this duality, by the IS monopole and dipole transitions, the inversion doublets having the $^{24}\mathrm{Mg}+\alpha$ and $^{20}\mathrm{Ne}+{}^{8}\mathrm{Be}$ configurations are excited as strongly as the single-particle estimates. Hence, it is concluded that the IS monopole and dipole transitions are regarded as a promising probe for these clustering.

This article is organized as follows. In the next section, the framework of AMD is briefly explained. The cluster S factor is also introduced as a measure of the clustering in the ground and excited states. In Sec. III, the intrinsic wave function obtained by the energy variation and the energy spectrum are presented. The systematics of the clustering in ^{28}Si is summarized. The relationship between the clustering in the excited states and the IS monopole and dipole transitions is discussed in Sec. IV. The final section summarizes this work.

II. FRAMEWORK

Here, the framework of AMD is briefly explained, and readers are directed to Refs. [45–47] for a detailed explanation.

A. Hamiltonian and variational wave function

The A-body microscopic Hamiltonian used in this study reads

$$H=\sum_{i}^{A}t_i-t_{c.m.}+\sum_{i<j}^{A}v_{ij}^{NN}+\sum_{i<j}^{A}v_{ij}^{\mathrm{Coul}}. \tag{1}$$

Here, t_i is kinetic energy of ith nucleon. $t_{c.m.}$ is the center-of-mass kinetic energy which is exactly subtracted without approximation in the AMD framework. We employ the Gogny D1S interaction [48] as an effective nuclear interaction, v^{NN}. The Coulomb interaction v^{Coul} is approximated by a sum of seven Gaussians.

The intrinsic wave function of AMD is an antisymmetrized product of nucleon wave packets φ_i,

$$\Phi_{\mathrm{int}}=\mathcal{A}\{\varphi_1\varphi_2\cdots\varphi_A\}, \tag{2}$$

where the nucleon wave packet is a direct product of the deformed Gaussian spatial part and the spin (χ_i) and isospin (ξ_i) parts:

$$\varphi_i(\boldsymbol{r})=\phi_i(\boldsymbol{r})\chi_i\xi_i, \tag{3}$$

$$\phi_i(\boldsymbol{r})=\exp\left\{-\sum_{\sigma=x,y,z}\nu_\sigma\left(r_\sigma-\frac{Z_{i\sigma}}{\sqrt{\nu_\sigma}}\right)^2\right\},$$

$$\chi_i=a_i\chi_\uparrow+b_i\chi_\downarrow,\quad \xi_i=\text{proton or neutron}. \tag{4}$$

The centroids of the Gaussian wave packet $\boldsymbol{Z}_i$, the direction of nucleon spin a_i,b_i, and the width parameter of the deformed Gaussian ν_σ are the variational parameters [3].

Before the energy variation, the intrinsic wave function is projected to the eigenstates of the parity,

$$\Phi^\pi=\frac{1+\pi P_x}{2}\Phi_{\mathrm{int}},\quad \pi=\pm. \tag{5}$$

Using this wave function, the variational energy is defined as

$$E^\pi=\frac{\langle\Phi^\pi|H|\Phi^\pi\rangle}{\langle\Phi^\pi|\Phi^\pi\rangle}+V_c. \tag{6}$$

By the frictional cooling method, the above-mentioned variational parameters are determined so that E^π is minimized. Here V_c is the potential which imposes the constraint on the variational wave function. In this study, we introduce two different constraint potentials. The first is the $\beta\gamma$ constraint, which is imposed on the quadrupole deformation of the variational wave function,

$$V_c=v_\beta(\langle\beta\rangle-\beta_0)^2+v_\gamma(\langle\gamma\rangle-\gamma_0)^2, \tag{7}$$

where $\langle\beta\rangle$ and $\langle\gamma\rangle$ are the quadrupole deformation parameters of the intrinsic wave function defined in Ref. [49], and v_β and

v_β are chosen large enough that $\langle\beta\rangle$ and $\langle\gamma\rangle$ are close to β_0 and γ_0 after the frictional cooling.

Another constraint is d constraint [50], which is imposed on the distance between *quasiclusters*,

$$V_c = v_d\big(\langle d^2\rangle - d_0^2\big)^2. \tag{8}$$

Similar to the $\beta\gamma$ constraint, v_d is chosen so that the squared distance between quasiclusters $\langle d^2\rangle$ is close to d_0^2 after the frictional cooling. The squared distance between quasiclusters is defined as follows. First, we select nucleons which belongs to each quasicluster. For example, in the case of the $\alpha + {}^{24}$Mg configuration, we choose four nucleon wave packets which belong to the α cluster and regard the remaining 24 wave packets as belonging to the ^{24}Mg cluster. Then, we define the center of mass of these quasiclusters as

$$\boldsymbol{R}_\alpha = \frac{1}{4}\sum_{i\in\alpha}\mathrm{Re}(\boldsymbol{Z}_i), \quad \boldsymbol{R}_{^{24}\mathrm{Mg}} = \frac{1}{24}\sum_{i\in{}^{24}\mathrm{Mg}}\mathrm{Re}(\boldsymbol{Z}_i), \tag{9}$$

and define $\langle d^2\rangle$ as the squared distance between those centers of mass,

$$\langle d^2\rangle = |\boldsymbol{R}_\alpha - \boldsymbol{R}_{^{24}\mathrm{Mg}}|^2. \tag{10}$$

Then we find the wave function which yields the minimum energy for given value of $\langle d^2\rangle$ by energy minimization. By applying this constraint, various kinds of cluster configurations have been studied [4,50–52]. In the present study, we calculated $\alpha + {}^{24}$Mg, ^{12}C + ^{16}O, and ^{8}Be + ^{20}Ne cluster configurations. It is noted that the d constraint is on the distance between the quasiclusters, not on their internal structure. As a result, when the intercluster distance is small, the clusters start to be strongly polarized to gain more binding energy, and the rearrangement of $\boldsymbol{Z}_i$ occurs. Further reduction of the intercluster distance dissociates the clusters and mean field is formed. Therefore, the clusters cannot be identified at shorter intercluster distance. On the other hand, with increase of the distance, the clusters approach their ground state configurations obtained by variations. In other words, this constraint smoothly connects the mean-field and cluster states as a function of the intercluster distance. This point will be discussed in Sec. III.

In the following, for the sake of simplicity, we denote the set of wave functions obtained by the above-mentioned constrained energy variations as Φ_i^π, where the subscript i is the index for each wave function. They are used as the basis wave functions for the generator coordinate method (GCM) calculation explained below.

B. Angular momentum projection and generator coordinate method

After the energy variation, we project the wave function to the eigenstate of the angular momentum:

$$\Phi^{J^\pi}_{MKi} = n\frac{2J+1}{8\pi^2}\int d\Omega\, D^{J*}_{MK}(\Omega)R(\Omega)\Phi_i^\pi, \tag{11}$$

where n, $D^J_{MK}(\Omega)$, and $R(\Omega)$ are the normalization factor, Wigner's D function, and the rotation operator, respectively. Then, they are superposed to describe the eigenstates of Hamiltonian,

$$\Psi_n^{J\pi} = \sum_{Ki} c_{Kin}\Phi^{J\pi}_{MKi} \tag{12}$$

The coefficient c_{Kin} is determined by solving the Hill-Wheeler equation (GCM) [53,54],

$$\sum_{K'j}\big\langle\Phi^{J\pi}_{MKi}\big|H\big|\Phi^{J\pi}_{MK'j}\big\rangle c_{K'jn} = E_n\sum_{K'j}\big\langle\Phi^{J\pi}_{MKi}\big|\Phi^{J\pi}_{MK'j}\big\rangle c_{K'jn}. \tag{13}$$

In the following, we call the thus-obtained wave function the GCM wave function.

In general, a GCM wave function given by Eq. (12) is a mixture of various cluster and noncluster configurations. Therefore, we introduce two measures to identify cluster states from the results of GCM calculations. The first measure is the overlap between the GCM wave function and the basis wave function,

$$O_i = \big|\big\langle\Psi_n^{J\pi}\big|\Phi_i^{J\pi}\big\rangle\big|^2. \tag{14}$$

If the overlap O_i with a certain $\Phi_i^{J\pi}$ is sufficiently large, the state described by $\Psi_n^{J\pi}$ may be interpreted to have the cluster configuration described by $\Phi_i^{J\pi}$.

To define a more quantitative measure, we introduce the projector to the cluster subspace. For example, the projector to the subspace spanned by the ^{16}O + ^{12}C configurations cluster is defined as

$$P_{^{16}\mathrm{O}+^{12}\mathrm{C}} = \sum_i \big|\Phi^{J^\pi}_{^{16}\mathrm{O}+^{12}\mathrm{C}}(d_j)\big\rangle B^{-1}_{ij}\big\langle\Phi^{J^\pi}_{^{16}\mathrm{O}+^{12}\mathrm{C}}(d_i)\big|, \tag{15}$$

$$B_{ij} = \big\langle\Phi^{J^\pi}_{^{16}\mathrm{O}+^{12}\mathrm{C}}(d_i)\big|\Phi^{J^\pi}_{^{16}\mathrm{O}+^{12}\mathrm{C}}(d_j)\big\rangle. \tag{16}$$

Here, $|\Phi^{J^\pi}_{^{16}\mathrm{O}+^{12}\mathrm{C}}(d)\rangle$ denote the wave functions having ^{16}O + ^{12}C cluster configurations with intercluster distance d obtained by applying the d constraint. The expectation value of $P_{^{16}\mathrm{O}+^{12}\mathrm{C}}$, which we call the cluster S factor in the following, is a good measure to know to what extent a GCM wave function is inside the ^{16}O + ^{12}C cluster subspace:

$$S_{^{16}\mathrm{O}+^{12}\mathrm{C}} = \big\langle\Psi_n^{J^\pi}\big|P_{^{16}\mathrm{O}+^{12}\mathrm{C}}\big|\Psi_n^{J^\pi}\big\rangle. \tag{17}$$

The cluster S factors for $^{24}\mathrm{Mg}+\alpha$, $^{20}\mathrm{Ne}+{}^{8}\mathrm{Be}$, and ^{16}O + ^{12}C configurations are also defined in the same manner. As already explained above, when the intercluster distance d is too small, the wave functions obtained by the d constraint do not have cluster structure. Therefore, we use the wave functions having nonsmall intercluster distance ($d \geqslant 4.0$ fm) to define the projectors.

III. RESULTS AND DISCUSSION

A. Result of energy variation

The energy surface of the $J^\pi = 0^+$ state obtained by the $\beta\gamma$ constraint and the angular momentum projection is shown in Fig. 1(a). There exist a couple of energy minima or plateaus with different quadrupole deformations. The lowest energy minimum has an oblate shape of $(\beta,\gamma) = (0.36, 46^\circ)$ with the

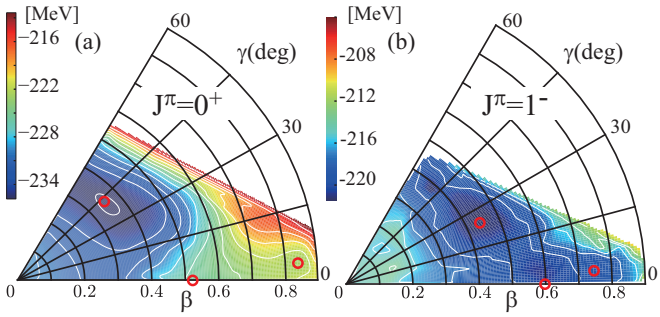

FIG. 1. The energy surfaces as functions of the quadrupole deformation parameters β and γ obtained by energy variation with the $\beta\gamma$ constraint and the angular momentum projection to (a) $J^\pi = 0^+$ and (b) $J^\pi = 1^-$. Red circles show the energy minima or plateaus.

energy $E = -235.7$ MeV, whose intrinsic density distribution is shown in Fig. 2(a). Around this global minimum, the energy surface is rather soft against both β and γ deformation. The second lowest state is prolately deformed, as seen in its intrinsic density distribution [Fig. 2(b)] and is located at $(\beta,\gamma) = (0.5,0^\circ)$ as a very shallow energy minimum. Those two energy minima indicate oblate and prolate shape coexistence in this nucleus and yield, respectively, the oblate deformed ground state and the prolate deformed 0^+_3 state by a GCM calculation. By further increasing the deformation, a third energy minimum with strongly elongated shape [Fig. 2(c)] appears at $(\beta,\gamma) = (0.85,5^\circ)$. As discussed in Ref. [4], this configuration has the $(sd)^8(pf)^4$ configuration and becomes the dominant component of the 0^+_4 state, which is regarded as the SD state.

The energy surface of the negative-parity $J^\pi = 1^-$ state shown in Fig. 1(b) does not have clear local minima, but there are three shallow minima or plateaus that are generated by the single-particle excitations. The global minimum is located at $(\beta,\gamma) = (0.43,27^\circ)$ with the energy $E = -221.2$ MeV. This

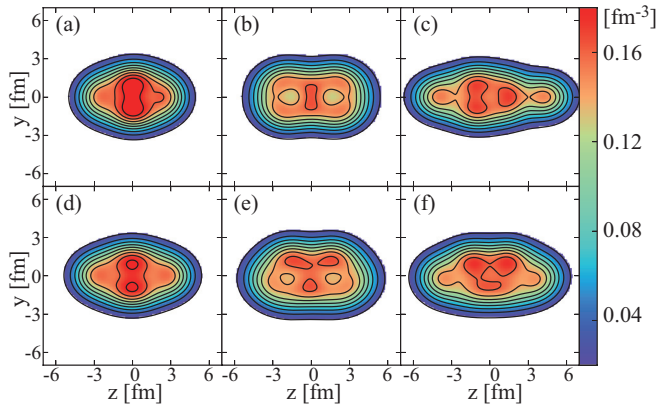

FIG. 2. Intrinsic matter density distributions of the minima on the positive- and negative-parity energy surfaces obtained by the $\beta\gamma$ constraint shown in Fig. 1. The panels (a), (b), and (c) show the oblate, prolate, and SD $J^\pi = 0^+$ minima, while the panels (d), (e), and (f) show the $J^\pi = 1^-$ minima generated by the 1p-1h excitations from the positive-parity minima.

configuration has a density distribution [Fig. 2(d)] similar to the oblate deformed ground state, because it is generated by the one-nucleon excitation from the ground state configuration. As shown in Figs. 2(e) and 2(f), there also exist prolate deformed and SD negative-parity minima that are generated by the 1p-1h excitations from the corresponding positive-parity minima. They are respectively located at $(\beta,\gamma) = (0.60,0^\circ)$ and $(0.73,2^\circ)$ with the energies $E = -220.8$ and -219.1 MeV. In terms of the Nilsson orbit, the prolate minimum is generated by the nucleon excitation from the $[Nn_zm_l\Omega^\pi] = [211\ 1/2^+]$ orbit to the $[330\ 1/2^-]$ orbit, while the negative-parity SD minimum is generated by the nucleon deexcitation from the $[330\ 1/2^-]$ orbit to the $[211\ 1/2^+]$ orbit.

As confirmed from the intrinsic density distributions shown in Fig. 2, the energy variation with the $\beta\gamma$ constraint does not generate prominent cluster configurations, but does generate mean-field configurations. On the other hand, the d constraint yields various cluster configurations. Figure 3 shows the energy curves obtained by the d constraint. In the previous study, the d constraint method was applied to the positive-parity states of the $^{24}\mathrm{Mg} + \alpha$ and the $^{16}\mathrm{O} + {}^{12}\mathrm{C}$ configurations. In addition to them, in the present study, we applied it to the $^{20}\mathrm{Ne} + {}^{8}\mathrm{Be}$ configuration and investigated both the positive and negative parities. As a result, we found that all of these cluster configurations appear in both parity states.

Figure 3(a) shows the energy curves for $^{24}\mathrm{Mg} + \alpha$ cluster configurations projected to the $J^\pi = 0^+$ and 1^- states. Because ^{24}Mg cluster is prolately deformed, two different $^{24}\mathrm{Mg} + \alpha$ configurations were obtained, in which the orientations of the ^{24}Mg cluster are different. In the configuration labeled $^{24}\mathrm{Mg} + \alpha$ (T), the longest axis of ^{24}Mg is perpendicular to the intercluster coordinate between ^{24}Mg and α clusters. As a result, the total system is triaxially deformed, as seen in its density distribution shown in Fig. 4(a). It is notable that, when the intercluster distance becomes small, the wave function of this configuration with $J^\pi = 0^+$ becomes almost identical to that of the oblate minimum on the $\beta\gamma$ energy surface (i.e., the ground state). The overlap between the wave functions of the $^{24}\mathrm{Mg} + \alpha$ (T) configuration and the oblate deformed ground state minimum [circles in Fig. 3(a)] has the maximum value 0.96 at $d = 2.0$ fm, and their energies are very close to each other (-235.7 and -234.5 MeV, respectively). Note that this does not necessarily mean that the ground state is clustered, but it means the equivalence of the cluster and shell model wave functions at small intercluster distance. This duality of shell and cluster is an essential ingredient for the enhanced monopole and dipole transitions discussed in Sec. IV.

To understood this point, the change of the $^{24}\mathrm{Mg} + \alpha$ (T) cluster configuration as a function of intercluster distance d is shown in Fig. 5. In the configurations with $d = 8.0$ and 4.0 fm [Figs. 5(a) and 5(b)], the α cluster can be clearly identified. The reduction of the intercluster distance dissociates the α cluster. It is slightly dissociated at $d = 3.0$ fm [Fig. 5(c)] and there is no clear indication of the α cluster at $d = 2.0$ fm [Fig. 5(d)]. It is completely dissociated at $d = 1.0$ fm [Fig. 5(e)] and the oblately deformed mean field is formed. As mentioned above, the configuration with $d = 2.0$ fm is almost identical to that of the oblate minimum in the $\beta\gamma$ energy surface. Thus, $^{24}\mathrm{Mg} + \alpha$ (T) cluster configuration is smoothly connected to

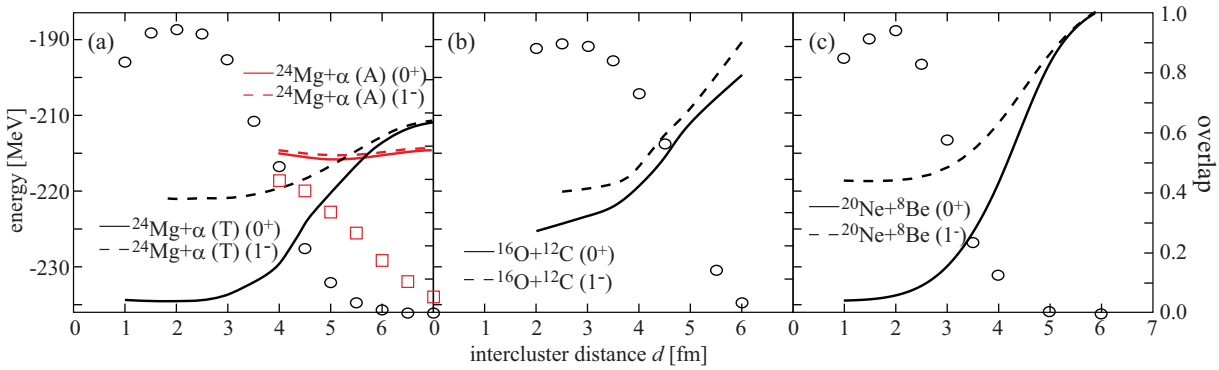

FIG. 3. Energy curves obtained by d constraint. Panels (a), (b), and (c) respectively show the energy curves of the $J^\pi = 0^+$ and 1^- states having $^{24}\mathrm{Mg} + \alpha$, $^{16}\mathrm{O} + {}^{12}\mathrm{C}$, and $^{20}\mathrm{Ne} + {}^{8}\mathrm{Be}$ configurations. Circles and boxes in the figure show the overlap between these $J^\pi = 0^+$ cluster configurations and the energy minima on the $\beta\gamma$ energy surface. Black circles in panels (a) and (c) shows the overlap between the oblate deformed minimum (ground state) and the $^{24}\mathrm{Mg} + \alpha$ (T) and $^{20}\mathrm{Ne} + {}^{8}\mathrm{Be}$ cluster configurations, while the red boxes in panel (a) show the overlap between the SD minimum and $^{24}\mathrm{Mg} + \alpha$ (A) configuration. The circles in panel (b) show the overlap between the prolate deformed minimum and the $^{12}\mathrm{C} + {}^{16}\mathrm{O}$ configuration.

the ground state configuration as a function of d. This implies that the degree of freedom of $^{24}\mathrm{Mg} + \alpha$ cluster excitation is embedded in the ground state configuration. To see this point quantitatively, we calculate the overlap between the wave functions of $^{24}\mathrm{Mg} + \alpha$ (T) configurations with and without distortions of clusters. To make the wave function without distortion, we shorten the intercluster distance of the wave function with $d = 8.0$ fm, shown in Fig. 5(a), to $d = 1.0$ fm by hand. The overlaps between thus-obtained wave function without the distortion and those with cluster distortion shown in Figs. 5(d) and 5(e) are 0.58 and 0.41, respectively. These large overlaps mean that the equivalence of the cluster and shell model wave functions still remains despite the distortion effect. This result ensures that the degree of freedom of the $^{24}\mathrm{Mg} + \alpha$ cluster is embedded in the ground state of ^{28}Si.

The negative-parity $J^\pi = 1^-$ state with the same $^{24}\mathrm{Mg} + \alpha$ (T) configuration [Fig. 4(e)] appears at a relatively high excitation energy that is approximately 15 MeV above the ground state. Differently from the $J^\pi = 0^+$ state, this negative-parity state has small overlap with the negative-parity minima in the $\beta\gamma$ energy surface, which amount to 0.20 at most. Other cluster configurations mentioned below also have small overlap with the mean field configurations. This means that the $\beta\gamma$ constraint and d constraint are describing the different classes of the negative-parity states. Namely, the $\beta\gamma$ constraint yields the single-particle excited states built on the mean field, while the d constraint yields the reflection-asymmetric cluster states in which the relative motion between clusters have odd angular momenta.

In another $^{24}\mathrm{Mg} + \alpha$ configuration, labeled $^{24}\mathrm{Mg} + \alpha$ (A), the longest axis of the ^{24}Mg cluster is parallel to the intercluster coordinate, and hence the system is axially deformed as shown in Fig. 4(b). This configuration with $J^\pi = 0^+$ has large overlap with the SD configuration shown in Fig. 2(c). The overlap between them amounts to 0.42 at the intercluster distance $d = 4.5$ fm. It is interesting to note that the negative-party $J^\pi = 1^-$ state [Fig. 4(f)] has almost the same intrinsic density distribution and almost the same energy as the positive-parity $J^\pi = 0^+$ state. This is because of the large intercluster distance

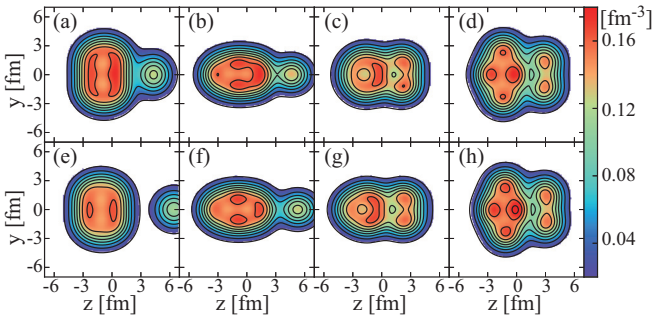

FIG. 4. Intrinsic matter density distributions obtained by d constraint. (a), (b), (c), and (d) respectively show the $^{24}\mathrm{Mg} + \alpha$ (T), $^{24}\mathrm{Mg} + \alpha$ (A), $^{16}\mathrm{O} + {}^{12}\mathrm{C}$, and $^{20}\mathrm{Ne} + {}^{8}\mathrm{Be}$ configurations with $J^\pi = 0^+$, while (e), (f), (g), and (h) show the $J^\pi = 1^-$ partners having the same configurations.

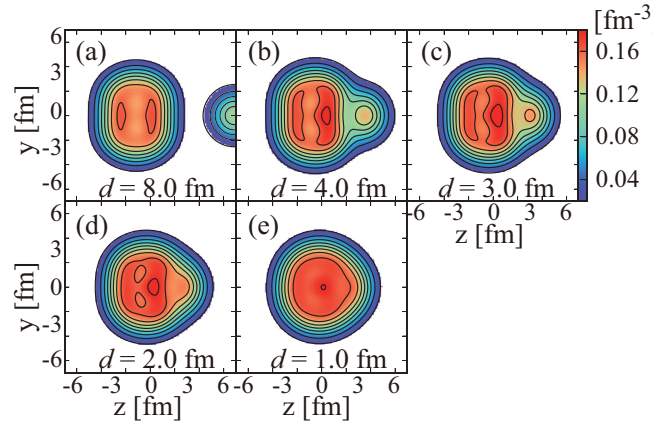

FIG. 5. Intrinsic matter density distributions obtained by d constraint for $^{24}\mathrm{Mg} + \alpha$ cluster configurations with various intercluster distance sd. (a), (b), (c), (d), and (e) show the configurations with $J^\pi = 0^+$ and $d = 8.0$, 4.0, 3.0, 2.0, and 1.0 fm, respectively.

of the the $^{24}\mathrm{Mg}+\alpha$ (A) configuration compared to the $^{24}\mathrm{Mg}+\alpha$ (T) configuration. The $^{24}\mathrm{Mg}+\alpha$ (A) configuration in negative parity does not have a corresponding state on the $\beta\gamma$ energy surface having large overlap.

The $^{16}\mathrm{O}+^{12}\mathrm{C}$ configuration with $J^\pi = 0^+$ appears approximately 10 MeV above the ground state with the intercluster distance $d = 2.5$ fm. At small intercluster distance, this configuration has large overlap with the prolate minimum located at $(\beta,\gamma) = (0.5,0^\circ)$ on the $\beta\gamma$ energy surface [Fig. 2(c)]. The overlap amounts to 0.90 at $d = 2.5$ fm. The negative-parity $J^\pi = 1^-$ state has an intrinsic density distribution similar to that of the positive-parity state, as shown in Fig. 4(g), and has an excitation energy close to its positive-parity partner. We also obtained another $^{16}\mathrm{O}+^{12}\mathrm{C}$ configuration having different orientation of the ^{12}C, which may correspond to the highly excited $^{16}\mathrm{O}+^{12}\mathrm{C}$ cluster states or molecular resonances [23–28]. However, its energy is rather high and it is not discussed here. Finally, we explain the $^{20}\mathrm{Ne}+^{8}\mathrm{Be}$ configuration. It has the triaxial intrinsic density distribution as shown in Fig. 4(d), in which the longest axes of ^{20}Ne and ^{8}Be clusters are parallel to each other, but perpendicular to the intercluster coordinate. At small intercluster distance, this configuration with $J^\pi = 0^+$ becomes identical to the oblate minimum on the $\beta\gamma$ energy surface (the ground state). Thus, the ground state and the $^{24}\mathrm{Mg}+\alpha$ and $^{20}\mathrm{Ne}+^{8}\mathrm{Be}$ cluster configurations have large overlap with each other at small intercluster distance. The negative-parity $J^\pi = 1^-$ state of $^{20}\mathrm{Ne}+^{8}\mathrm{Be}$ configuration appears at approximately 17 MeV above the ground state with the intercluster distance $d = 3.0$ fm.

The result of the energy variation is summarized as follows. (1) The $\beta\gamma$ constraint yielded three mean-field configurations with $J^\pi = 0^+$ having oblate, prolate, and SD shapes. The oblate minimum has the lowest energy and corresponds to the ground state, while the others constitute the excited 0^+ states. (2) The d constraint yielded prominent $^{24}\mathrm{Mg}+\alpha$ (T) and (A), $^{16}\mathrm{O}+^{12}\mathrm{C}$, and $^{20}\mathrm{Ne}+^{8}\mathrm{Be}$ cluster configurations with large intercluster distance, and smoothly connects them to the mean-field states at small intercluster distance. These cluster configurations have large overlap with the mean-field configurations, indicating that the prolate, oblate, and SD minima on the $\beta\gamma$ energy surface have duality of shell and cluster. Namely, the oblate deformed ground state has the duality of $^{24}\mathrm{Mg}+\alpha$ (T) and $^{20}\mathrm{Ne}+^{8}\mathrm{Be}$ cluster configurations. The prolate minimum has the duality of the $^{16}\mathrm{O}+^{12}\mathrm{C}$ configuration and the SD minimum has the duality of the $^{24}\mathrm{Mg}+\alpha$ (A) configuration. (3) All of the cluster configurations are accompanied by the negative-parity partner having almost the same intrinsic density distributions. These negative-parity states originate in their reflection-asymmetric cluster configurations.

B. Excitation spectrum and clustering

1. *Overview of the spectrum*

Figure 6 shows the energy levels obtained by the GCM calculation together with the corresponding observed states. In the figure, the rotational bands which have sizable amounts of the cluster S factors and overlaps with the cluster wave functions are shown. Other excited states are omitted, except for the β band built on the ground-state band. Experimentally, several candidates of cluster states with same spin-parity are observed [19,22]. The situation is same in our result. Namely, there are several states which have the same spin-parity and sizable cluster S factors. For these states, their energies are averaged and shown by dashed lines in Fig. 6 to illustrate the clustering systematics more transparently. The detailed distribution of the cluster S factors in the excited states is discussed in Sec. IV.

The results for the positive-parity states are consistent with our previous study, and we find that most of the positive-parity bands are accompanied by the negative-parity bands because of their duality of mean-field and reflection-asymmetric clustering. The present result is briefly summarized as follows. The oblate minimum on the $\beta\gamma$ energy surface and the $^{24}\mathrm{Mg}+\alpha$ (T) configuration are mixed with each other and generate a group of rotational bands labeled $^{24}\mathrm{Mg}+\alpha$ (T) bands in Fig. 6. The oblate minimum also mixed with the $^{20}\mathrm{Ne}+^{8}\mathrm{Be}$ configuration to generate a pair of the positive- and negative-parity bands labeled $^{20}\mathrm{Ne}+^{8}\mathrm{Be}$ doublet. In a similar way, the prolate deformed minimum is mixed with the $^{16}\mathrm{O}+^{12}\mathrm{C}$ configuration, and the SD minimum is mixed with the $^{24}\mathrm{Mg}+\alpha$ (A) configuration. As a result, they respectively

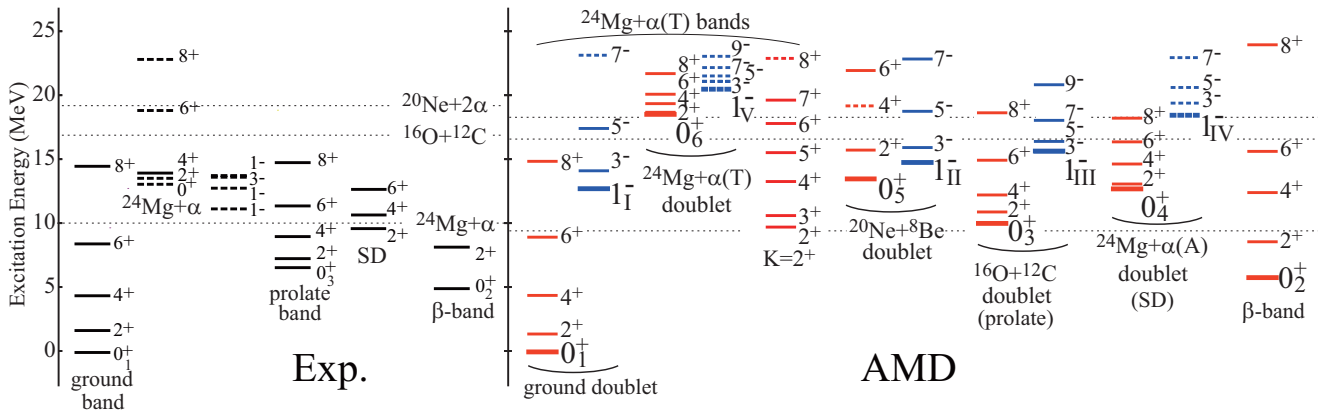

FIG. 6. Calculated and observed partial level scheme of ^{28}Si. The levels shown by dashed lines are the averaged energies for the candidates of cluster states. Dotted lines show the experimental and theoretical $^{24}\mathrm{Mg}+\alpha$, $^{16}\mathrm{O}+^{12}\mathrm{C}$, and $^{20}\mathrm{Ne}+2\alpha$ threshold energies.

TABLE I. The calculated in-band $B(E2)$ ($e^2\text{fm}^4$) strengths in the ground state, $^{24}\text{Mg}+\alpha$ (T), $^{20}\text{Ne}+{}^{8}\text{Be}$, $^{16}\text{O}+{}^{12}\text{C}$, $^{24}\text{Mg}+\alpha$ (A) doublets and in the β band. The numbers in parentheses are the experimental data [17].

	Ground	$^{24}\text{Mg}+\alpha$ (T)	$^{20}\text{Ne}+{}^{8}\text{Be}$
$B(E2;2^+\to 0^+)$	79.4 (67)	29.2	15.3
$B(E2;4^+\to 2^+)$	123 (83)	28.9	12.7
$B(E2;3^-\to 1^-)$	94.9	24.9	18.3
$B(E2;5^-\to 3^-)$	111	27.2	10.8
	$^{16}\text{O}+{}^{12}\text{C}$	$^{24}\text{Mg}+\alpha$ (A)	β band
$B(E2;2^+\to 0^+)$	221	664	52.8
$B(E2;4^+\to 2^+)$	299 (150)	939	69.7
$B(E2;3^-\to 1^-)$	244	409	
$B(E2;5^-\to 3^-)$	382	424	

generate pairs of the positive- and negative-parity bands, which are labeled $^{16}\text{O}+{}^{12}\text{C}$ and $^{24}\text{Mg}+\alpha$ (A) doublets. In addition to them, the positive-parity band labeled β band is generated by the β vibration of the ground-state band.

2. $^{24}\text{Mg}+\alpha$ (T) bands

A group of the rotational bands labeled $^{24}\text{Mg}+\alpha$ (T) bands includes three positive-parity bands and two negative-parity bands. The positive-parity bands are the ground-state band ($K^\pi=0^+$), the $K^\pi=2^+$ band, and another $K^\pi=0^+$ band built on the 0^+_6 state at 18.2 MeV. Because of the reflection-asymmetric clustering of the $^{24}\text{Mg}+\alpha$ (T) configuration, two negative-parity $K^\pi=0^-$ bands built on the 1^-_{I} and 1^-_{IV} are paired with the $K^\pi=0^+$ bands to constitute two parity doublets, which are labeled the ground doublet and $^{24}\text{Mg}+\alpha$ (T) doublet in the figure.

The ground-state band is dominated by the oblately deformed mean-field configuration shown in Fig. 2(a) whose overlap with the GCM wave function amounts to 0.84. The moments of inertia of the ground-state band and the $B(E2)$ strengths listed in Table I reasonably agree with the observed data, indicating that the deformed mean-field nature of the ground state is properly described by the present calculation. However, it must be noted that this ground-state band also has a large overlap with the $^{24}\text{Mg}+\alpha$ (T) configuration with small intercluster distance, which amount to 0.96 for $d=2.0$ fm. This means that the ground-state band has a duality of the oblate shaped mean-field and $^{24}\text{Mg}+\alpha$ (T) clustering. Therefore, the excitation of the intercluster motion between ^{24}Mg and α clusters yields excited bands with prominent clustering. The $1\hbar\omega$ excitation of the intercluster motion yields the $K^\pi=0^-$ band built on the 1^- state labeled 1^-_{I}, which is dominated by the negative-parity $^{24}\text{Mg}+\alpha$ (T) configuration with $d=2.5$ fm. Hence, we assigned it as the partner of the ground-state band which constitutes the ground doublet, although the 1p-1h mean-field configuration [Fig. 2(d)] also has non-negligible contribution to this band. In addition to the ground doublet, the $2\hbar\omega$ and $3\hbar\omega$ excitations of the intercluster motion yield $K^\pi=0^\pm$ bands built on the 0^+_6 state and a group of 1^- states labeled 1^-_{V}, which constitute another doublet labeled $^{24}\text{Mg}+\alpha$ (T) doublet. Because of the coupling with other noncluster configurations, the $^{24}\text{Mg}+\alpha$ (T) configuration does not appear as a single 1^- state but appears as three 1^- states located at 20.6, 21.5, and 22.5 MeV. As the excitation energy becomes large, these 1^- states tend to have larger intercluster distance, as shown in Sec. IV. To illustrate the band structure clearly, their excitation energies are averaged and labeled as 1^-_{V} in Fig. 6. As the intercluster motion is largely excited, these bands have prominent cluster structure. The 0^+_6 and 1^-_{V} states have large overlap with the configurations shown in Figs. 4(a) and 4(e), which amount to 0.32 and 0.22 (averaged), respectively. In addition to these parity doublets, the triaxial deformation of the $^{24}\text{Mg}+\alpha$ (T) configuration yields $K^\pi=2^+$ band. Thus, the duality of the ground state yields two parity doublets and the $K^\pi=2^+$ band which are classified as $^{24}\text{Mg}+\alpha$ (T) bands.

3. $^{20}\text{Ne}+{}^{8}\text{Be}$ doublet and β band

As discussed in Sec. III A, the oblate deformed minimum also has large overlap with the $^{20}\text{Ne}+{}^{8}\text{Be}$ configuration with small intercluster distance. Therefore, the excitation of the intercluster motion between ^{20}Ne and ^{8}Be clusters should yield a series of the cluster bands. In addition, the deformed mean-field aspect of the ground state can yield a different kind of excitation mode, i.e., the β vibration. The GCM calculation showed that these two excitation modes strongly mix with each other to yield the 0^+_2 and 0^+_5 states. Their overlaps with the configurations shown in Fig. 4(d) amount to 0.13 and 0.18, respectively. Similarly to the $^{24}\text{Mg}+\alpha$ configuration, the $^{20}\text{Ne}+{}^{8}\text{Be}$ configuration yields the 1^-_{II} state, which is paired with the 0^+_5 state to constitute the parity doublet labeled $^{20}\text{Ne}+{}^{8}\text{Be}$ doublet.

4. $^{16}\text{O}+{}^{12}\text{C}$ doublet and $^{24}\text{Mg}+\alpha$ (A) doublet

In addition to the above-mentioned bands related to the ground state duality, there are other bands which are unrelated to the ground state. The prolate band is built on the 0^+_3 state at 10.0 MeV, which has a large overlap with the prolate deformed local minimum shown in Fig. 2(b). Combined with the oblately deformed ground state, this prolate deformed 0^+_3 state indicates the shape coexistence in the low-lying states of ^{28}Si. As discussed in the previous work [4], this prolate band has large overlap with the $^{16}\text{O}+{}^{12}\text{C}$ cluster configuration. Hence, it is concluded that the prolate band has the duality of the prolate deformed mean-field and $^{16}\text{O}+{}^{12}\text{C}$ clustering. The negative-parity band built on the 1^-_{III} state also has a large overlap with the $^{16}\text{O}+{}^{12}\text{C}$ configuration [Fig. 4(g)], and is assigned as the partner of the positive-parity prolate band, that constitutes the $^{16}\text{O}+{}^{12}\text{C}$ doublet.

Another prolate deformed minimum, i.e., the SD minimum located at $(\beta,\gamma)=(0.85,5^\circ)$ generates the SD band built on the 0^+_4 state at 12.7 MeV. This band has large overlap with the $^{24}\text{Mg}+\alpha$ (A) configuration shown in Fig. 4(f). The corresponding negative-parity partner dominated by the $^{24}\text{Mg}+\alpha$ (A) configuration exists. However, it does not appear as a single 1^- state but as two 1^- states around 17.5 and 18.8 MeV because of the coupling with the $^{16}\text{O}+{}^{12}\text{C}$

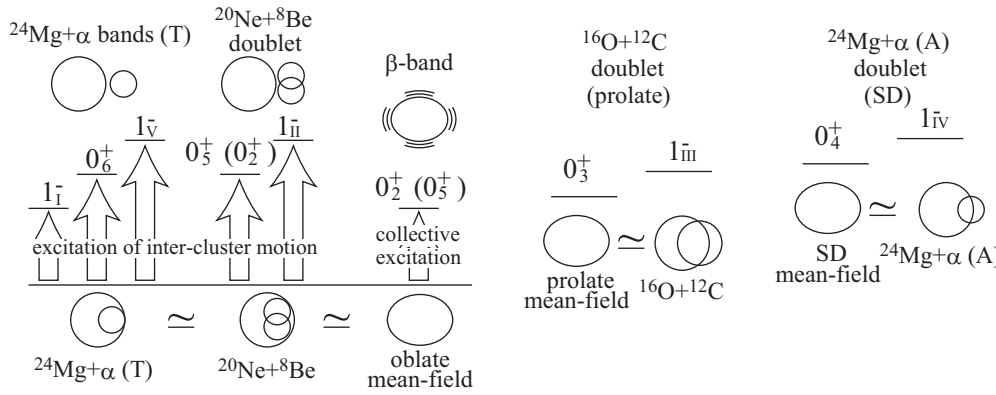

FIG. 7. The oblate deformed ground state has the duality of the mean field and $^{24}\mathrm{Mg}+\alpha$ (T) and $^{16}\mathrm{O}+{}^{12}\mathrm{C}$ clustering. From the duality, the β band, $^{24}\mathrm{Mg}+\alpha$ bands, and $^{20}\mathrm{Ne}+{}^{8}\mathrm{Be}$ doublet arise.

configuration. The lower energy state (17.5 MeV) has a shorter intercluster distance of the $^{24}\mathrm{Mg}+\alpha$ (A) configuration, while the higher energy one (18.8 MeV) has a longer intercluster distance. In Fig. 6, their averaged energy is labeled 1^-_{IV}, and the negative-parity band built on these states is associated with the positive-parity band. We denote this doublet as $^{24}\mathrm{Mg}+\alpha$ (A) doublet. As discussed in the previous section, the $^{16}\mathrm{O}+{}^{12}\mathrm{C}$ and $^{24}\mathrm{Mg}+\alpha$ (A) configurations do not overlap with the oblate deformed ground state. Therefore, the $^{16}\mathrm{O}+{}^{12}\mathrm{C}$ and $^{24}\mathrm{Mg}+\alpha$ (A) doublets are disconnected from the ground state.

5. *Systematics of clustering and observed candidates*

To summarize this section, the systematics of the cluster states explained above is schematically illustrated in Fig. 7. The ground state has duality of the oblate deformed mean-field, $^{24}\mathrm{Mg}+\alpha$ (T), and $^{20}\mathrm{Ne}+{}^{8}\mathrm{Be}$ cluster configurations. The excitation of the intercluster motion between $^{24}\mathrm{Mg}$ and α clusters yields a group of $^{24}\mathrm{Mg}+\alpha$ (T) bands. The $^{20}\mathrm{Ne}+{}^{8}\mathrm{Be}$ clustering also arises from the ground state duality, and it is strongly mixed with the β-vibration mode which arises from the mean-field aspect of the ground state. Aside from these bands, the $^{16}\mathrm{O}+{}^{12}\mathrm{C}$ and $^{24}\mathrm{Mg}+\alpha$ (A) doublets exist and are disconnected from the ground state, because of the orthogonality of their cluster configurations to the ground state.

Experimentally, the three low-lying positive-parity bands, i.e., the ground-state band, β band, and the prolate band, are assigned firmly and coincide with the present calculation, although the calculation slightly overestimates the energies of the excited bands. On the other hand, the experimental assignments of the negative-parity bands and high-lying bands are not established yet, and hence, the assignment of the cluster bands is still ambiguous. Many experiments have been performed to identify the cluster bands [17–23], and Fig. 6 shows the candidates of the cluster bands reported in Refs. [17,19,22], which energetically coincide with the present calculation. A couple of $0^+,2^+$ and $1^-,3^-$ states were reported around $E_x = 13$ MeV by the α transfer and radiative α capture reactions. They have relatively large α decay width, hence they can be regarded as candidates of the $^{24}\mathrm{Mg}+\alpha$ (T) or $^{24}\mathrm{Mg}+\alpha$ (A) doublets. Furthermore, based on the analysis of the $^{24}\mathrm{Mg}(\alpha,\gamma)$ and $^{12}\mathrm{C}(^{20}\mathrm{Ne},\alpha)^{28}\mathrm{Si}$ reactions, another rotational band was suggested [17], and the authors assigned it to the SD band predicted by the previous AMD study [4].

IV. ISOSCALAR MONOPOLE AND DIPOLE TRANSITIONS

Here, we discuss that part of the clustering systematics summarized above can be detected by the IS monopole and dipole transitions from the ground state. To illustrate this, we first discuss the duality of shell and cluster, based on the SU(3) shell model [43,44] and Bayman-Bohr theorem [55,56]. In the case of $^{28}\mathrm{Si}$, the ground state deviates from a pure SU(3) shell model state because of the strong influence of the spin-orbit interaction. To take this into account, the evaluation of the transition strengths by the realistic nuclear model is indispensable for quantitative discussions. For this purpose, we present the result of AMD calculation to show that the IS monopole and dipole transitions strongly yield cluster states.

A. Duality of shell and cluster

In Sec. III, we have explained that many low-lying positive-parity states have the duality of the mean-field (shell) and cluster. Here, we show that this is reasonably understood using the SU(3) shell model [43,44] and the Bayman-Bohr theorem [55,56].

$^{28}\mathrm{Si}$ has 12 nucleons in the sd shell on top of the $^{16}\mathrm{O}$ core, and its oblate deformed ground state can be approximated by the $(\lambda,\mu) = (0,12)$ representation of the SU(3) shell model. Denoting the eigenstates of three-dimensional harmonic oscillator in the Cartesian representation $(n_x n_y n_z)$, it is written as

$$(\lambda,\mu) = (0,12): \ (002)^4(011)^4(020)^4, \tag{18}$$

where the configuration of 12 nucleons is explicitly shown, and the $^{16}\mathrm{O}$ core which corresponds to $(000)^4(100)^4(010)^4(001)^4$ is omitted.

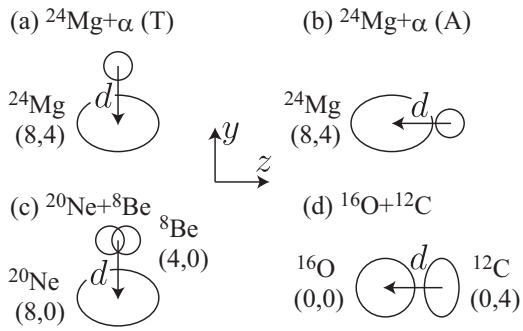

FIG. 8. Schematic figure for the various cluster configurations and their duality.

In a same manner, the prolate deformed state is approximated by the $(\lambda,\mu) = (12,0)$ representation

$$(\lambda,\mu) = (12,0) : \ (002)^4(011)^4(101)^4, \tag{19}$$

in which the orbit occupied by the last four nucleons is different from that in the ground state. The excitation of the last four nucleons into the pf shell yields the SD configuration which is given by the $(\lambda,\mu) = (20,4)$ representation.

$$(\lambda,\mu) = (20,4) : \ (002)^4(011)^4(003)^4. \tag{20}$$

The Bayman-Bohr theorem tells us that these SU(3) shell model wave functions are identical to the cluster model wave functions with zero intercluster distance. First, we consider $^{24}\mathrm{Mg} + \alpha$ cluster configurations. The triaxially deformed ground state of ^{24}Mg is given by the $(\lambda,\mu) = (8,4)$ representation,

$$(\lambda,\mu) = (8,4) : \ (002)^4(011)^4, \tag{21}$$

where the longest deformation axis is the z axis. Now we consider the $^{24}\mathrm{Mg} + \alpha$ configuration in which the α cluster is placed on the y axis as illustrated in Fig. 8(a). This configuration corresponds to the $^{24}\mathrm{Mg} + \alpha$ (T) configuration obtained by AMD calculation. Since the orbits (000) and (010) are already occupied by the nucleons in the ^{24}Mg cluster, the nucleons in the α cluster having $(000)^4$ configuration must occupy $(020)^4$ at zero intercluster distance $d = 0$. As a result, one sees that the $^{24}\mathrm{Mg} + \alpha$ (T) cluster configuration becomes identical to the (0,12) representation for the ground state given by Eq. (19),

$$\lim_{d\to 0} \Phi_{^{24}\mathrm{Mg}+\alpha(\mathrm{T})}(d) = (002)^4(011)^4(020)^4. \tag{22}$$

This clearly explains why the $^{24}\mathrm{Mg} + \alpha$ (T) configuration obtained by the d constraint becomes almost identical to the ground state configuration at small intercluster distance d. The placement of the α particle on the z axis corresponds the another configuration $^{24}\mathrm{Mg} + \alpha$ (A) as shown in Fig. 8(b). In this case, at zero intercluster distance, the nucleons in the α cluster occupy $(003)^4$, resulting in the SD configuration given by Eq. (20),

$$\lim_{d\to 0} \Phi_{^{24}\mathrm{Mg}+\alpha(\mathrm{A})}(d) = (002)^4(011)^4(003)^4. \tag{23}$$

The other cluster configurations are also considered in the same way. The prolately deformed ground state of ^{20}Ne is given by the $(\lambda,\mu) = (8,0)$ representation,

$$(\lambda,\mu) = (8,0) : \ (002)^4, \tag{24}$$

where the symmetry axis of ^{20}Ne is the z axis. The $^{20}\mathrm{Ne} + {}^{8}\mathrm{Be}$ configuration corresponds to the placement of the ^{8}Be cluster on the y axis where the symmetry axis of ^{8}Be is also the z axis [Fig. 8(c)]. At zero intercluster distance, the nucleons in the ^{8}Be cluster having $(000)^4(001)^4$ configuration occupy $(020)^4(011)^4$ due to the Pauli principle, and one finds it is identical to the ground state configuration,

$$\lim_{d\to 0} \Phi_{^{20}\mathrm{Ne}+{}^{8}\mathrm{Be}}(d) = (002)^4(011)^4(020)^4. \tag{25}$$

The oblately deformed ground state of ^{12}C is given by the $(\lambda,\mu) = (0,4)$ representation,

$$(\lambda,\mu) = (0,4) : \ (000)^4(100)^4(010)^4, \tag{26}$$

where the symmetry axis is the z axis. The $^{16}\mathrm{O} + {}^{12}\mathrm{C}$ configuration corresponds the placement of ^{16}O and ^{12}C clusters on the z axis as shown in Fig. 8(d). At zero intercluster distance, it is identical to the prolate deformed state,

$$\lim_{d\to 0} \Phi_{^{16}\mathrm{O}+{}^{12}\mathrm{C}}(d) = (002)^4(011)^4(101)^4. \tag{27}$$

Thus, considering the corresponding SU(3) shell model wave function, the duality of the mean-field and cluster configurations illustrated in Fig. 7 is clearly explained. It is also noted that the duality of the shell and cluster in ^{28}Si was also investigated and found by a Skyrme Hartree-Fock calculation [11].

As discussed in Refs. [39,40,42], this duality of shell and cluster means that the degrees of freedom of $^{28}\mathrm{Mg} + \alpha$ (T) and $^{20}\mathrm{Ne} + {}^{8}\mathrm{Be}$ cluster excitations are embedded in the ground state. Therefore, the excitation of the intercluster motion embedded in the ground state yields excited cluster states with pronounced $^{24}\mathrm{Mg} + \alpha$ (T) and $^{20}\mathrm{Ne} + {}^{8}\mathrm{Be}$ configurations. The important fact is that the IS monopole and dipole transitions between the ground state and these excited cluster states are very strong, and hence these transitions are a very good probe for the clustering. Indeed, if one assumes that the ground state is a pure SU(3) shell model state and the excited cluster states are described by the cluster model wave function, it is possible to analytically show the enhancement of the IS monopole and dipole transitions [39,42]. However, in the case of ^{28}Si, the ground state deviates from a pure SU(3) shell model state because of the strong influence of the spin-orbit interaction. In addition to this, the coupling between the cluster configurations and mean-field configurations in the excited states is not negligible. Therefore, the evaluation of the transition strengths by the realistic nuclear model is indispensable for quantitative discussions. For this purpose, we present the results of the GCM calculation below.

B. Isoscalar monopole and dipole transitions

Using the wave functions of the ground and excited cluster states obtained by the GCM calculation, the IS monopole and dipole transition strengths are directly evaluated. The transition operators and matrix elements between the ground and excited

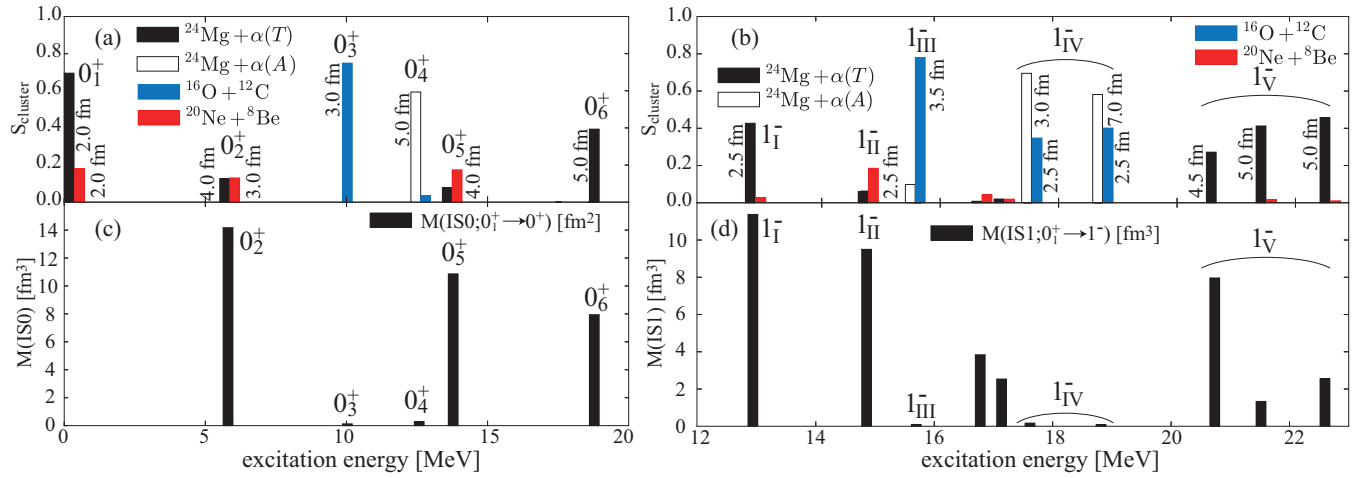

FIG. 9. (a) The cluster S factors for the ground and excited 0^+ states. (b) Same as (a) but for the excited 1^- states. (c) The IS monopole transition matrix from the ground state to the excited 0^+ states. (d) The IS dipole transition matrix from the ground state to the excited 1^- states. The values indicate the intercluster distance of the configuration which has the largest overlap in units of fm.

states are given as

$$\mathcal{M}(IS0) = \sum_{i=1}^{A}(\boldsymbol{r}_i - \boldsymbol{r}_{\rm cm})^2, \tag{28}$$

$$\mathcal{M}_\mu(IS1) = \sum_{i=1}^{A}(\boldsymbol{r}_i - \boldsymbol{r}_{\rm cm})^2 \mathcal{Y}_{1\mu}(\boldsymbol{r}_i - \boldsymbol{r}_{\rm cm}), \tag{29}$$

$$M(IS0; 0^+_1 \to 0^+_n) = \langle 0^+_n|\mathcal{M}(IS0)|0^+_1\rangle, \tag{30}$$

$$M(IS1; 0^+_1 \to 1^-_n) = \langle 1^-_n||\mathcal{M}_0(IS1)||0^+_1\rangle = \sqrt{3}\langle 1^-_n|\mathcal{M}_0(IS1)|0^+_1\rangle, \tag{31}$$

where $\boldsymbol{r}_i$ and $\boldsymbol{r}_{\rm cm}$ denote the single-particle and center-of-mass coordinates, respectively. The solid spherical harmonics is defined as $\mathcal{Y}_{1\mu}(\boldsymbol{r}) = rY_{1\mu}(\hat{r})$. We also calculated the cluster S factors of the ground and exited states to see how the clustering and IS monopole and dipole transitions are correlated to each other.

The results are shown in Fig. 9, where panels (a) and (b) show the cluster S factors and of 0^+ and 1^- states while panels (c) and (d) shows the IS monopole and dipole transition matrices. The inter-cluster distances of the configuration which has the largest overlap are also shown in the panels (a) and (b). The calculated S factors confirm the clustering systematics summarized in Fig. 7. Owing to the duality of the shell and cluster, the ground state has a large S factor for the ^{24}Mg + α (T) configuration, which amounts to 0.68, and has a non-negligible S factor for the ^{20}Ne + ^{8}Be configuration. The 0^+_6 state is regarded as the pronounced ^{24}Mg + α (T) cluster state, while the $0^+_5(0^+_2)$ state is regarded as the pronounced ^{20}Ne + ^{8}Be cluster states from their S factors. One also sees that the $1^-_{\rm I}$ state and a group of 1^- states labeled $1^-_{\rm V}$ are the ^{24}Mg + α (T) cluster states and are paired with the ground state and the 0^+_6 state, respectively, while the $1^-_{\rm II}$ state should be paired with the 0^+_5 state to constitute the ^{20}Ne + ^{8}Be doublet. In the same way, the S factors clearly show that the 0^+_3 and $1^-_{\rm III}$ states are the ^{16}O + ^{12}C doublet and the 0^+_4 and $1^-_{\rm IV}$ states are the ^{24}Mg + α (A) doublet, although the ^{16}O + ^{12}C configuration is also mixed in the $1^-_{\rm IV}$ states.

The intercluster distances of the cluster configurations having the largest overlaps with the 0^+ and 1^- states also support the clustering systematics shown in Fig. 7. The ground state has the largest overlap with the ^{24}Mg + α (T) and ^{20}Ne + ^{8}Be cluster configurations of 2 fm inter-cluster distance. This short distance indicates the duality of the shell and cluster in the ground state. On the other hand, the excited states have larger intercluster distance. For example, the 0^+_6 state has largest overlap with the ^{24}Mg + α (T) configuration of 5.0 fm inter-cluster distance, and the group of 1^- states labeled 1^-_V has the largest overlap with the ^{24}Mg + α (T) configuration of 4.5–5.5 fm intercluster distance. From this fact, we assigned the 0^+_6 and 1^-_V states as the ^{24}Mg + α (T) doublet. In the same way, one can find that the 0^+_4 and 1^-_{IV} states should be assigned as the ^{24}Mg + α (A) doublet. Figure 9 also shows that two of the three 1^- states which constitute the 1^-_V have larger intercluster distance than the lowest energy one. The situation is common to the 1^-_{IV}, i.e., the highly excited state has larger inter-cluster distance.

It is very impressive to see that the IS monopole and dipole strengths shown in panels (c) and (d) are very strongly correlated to the S factors for the ^{24}Mg + α (A) and ^{20}Ne + ^{8}Be configurations, but are almost insensitive to the other cluster and noncluster states except for a couple of 1^- states around 17 MeV. Because the IS monopole and dipole operators activate the degree of freedom of cluster excitation embedded in the ground state, the transition strengths to the ^{24}Mg + α (A) and ^{20}Ne + ^{8}Be cluster states are as strong as the single-particle estimates, which are given as

$$M(IS0)_{WU} = \frac{3}{5}(1.2A^{1/3})^2 \simeq 8.0\ {\rm fm}^2 \tag{32}$$

$$M(IS1)_{WU} = \sqrt{\frac{3}{16\pi}}(1.2A^{1/3})^3 \simeq 11.8\ {\rm fm}^2. \tag{33}$$

Therefore, we can conclude that the IS monopole and dipole transitions are a good probe to identify the ^{24}Mg + α (T) and ^{20}Ne + ^{8}Be clustering.

Recently, interesting and promising experimental data were reported by the measurement of ^{28}Si(α,α')^{28}Si* inelastic scattering [57,58]. It was found that a couple of 0^{+} states above 9 MeV are strongly populated and were deduced to have large IS monopole transition strengths. Hence, they are suggested as strong candidates of the α cluster states [58]. We expect that a detailed comparison of the IS monopole and dipole transition strengths between experiment and theory will reveal the clustering systematics in ^{28}Si.

V. SUMMARY

In summary, we have investigated the clustering systematics in ^{28}Si based on the antisymmetrized molecular dynamics. It is found that the inversion doublet bands with various kinds of reflection-asymmetric cluster configuration appear in the excited states, and the IS monopole and dipole transitions are a good probe for ^{24}Mg + α (T) and ^{20}Ne + ^{8}Be cluster states.

The energy variation by using the d constraint yielded various kinds of cluster configurations with positive and negative parity, while the $\beta\gamma$ constraint yielded mean-field configurations. It is found that the cluster configurations become identical to the mean-field configurations at small intercluster distance because of the duality of mean-field (shell) and cluster. In particular, it is emphasized that the oblate deformed ground state has the duality of the ^{24}Mg + α (T) and ^{20}Ne + ^{8}Be configurations.

The GCM calculation showed that a group of the ^{24}Mg + α (T) and ^{20}Ne + ^{8}Be cluster bands are generated by the excitation of the intercluster motion embedded in the ground state. In addition to them, the prolate and SD bands have the duality of ^{16}O + ^{12}C and ^{20}Ne + ^{8}Be clustering, respectively. Because of their reflection-asymmetric intrinsic configurations, they are accompanied by the negative-parity bands to constitute the inversion doublets.

Because of the duality of the ground state, it is numerically shown that the ^{24}Mg + α (T) and ^{20}Ne + ^{8}Be cluster bands have enhanced IS monopole and dipole transition matrices which are as large as the single-particle estimates. On the other hand, other cluster states and noncluster states are rather insensitive to the IS monopole and dipole transitions. Hence, we conclude that the ^{24}Mg + α (T) and ^{20}Ne + ^{8}Be cluster bands can be identified from their enhanced transitions. We expect that a more quantitative comparison with the experiments will reveal the clustering systematics in ^{28}Si.

ACKNOWLEDGMENTS

The authors thank Prof. Kanada-En'yo, Prof. Kawabata, and Prof. Ito for the fruitful discussions. Part of the numerical calculations were performed by using the supercomputers at the High Energy Accelerator Research Organization (KEK) and at the Yukawa Institute for Theoretical Physics (YITP) of Kyoto University. Support by Grants-in-Aid for Scientific Research on Innovative Areas from MEXT (Grant No. 2404:24105008) and JSPS KAKENHI Grants No. 16J03654, No. 25800124, and No. 16K05339 are acknowledged.

[1] Y. Fujiwara, H. Horiuchi, K. Ikeda, M. Kamimura, K. Kato, Y. Suzuki, and E. Uegaki, Prog. Theor. Phys. Suppl. **68**, 29 (1980).
[2] M. Kimura and H. Horiuchi, Phys. Rev. C **69**, 051304 (2004).
[3] M. Kimura, Phys. Rev. C **69**, 044319 (2004).
[4] Y. Taniguchi, Y. Kanada-En'yo, and M. Kimura, Phys. Rev. C **80**, 044316 (2009).
[5] S. Das Gupta and M. Harvey, Nucl. Phys. A **94**, 602 (1967).
[6] F. Glatz, P. Betz, J. Siefert, F. Heidinger, and H. Röpke, Phys. Rev. Lett. **46**, 1559 (1981).
[7] F. Glatz, J. Siefert, P. Betz, E. Bitterwolf, A. Burkard, F. Heidinger, T. Kern, R. Lehmann, S. Norbert, and H. Röpke, Z. Phys. A **303**, 239 (1981).
[8] R. K. Sheline, S. Kubono, K. Morita, and M. Tanaka, Phys. Lett. B **119**, 263 (1982).
[9] J. Cseh and W. Scheid, J. Phys. G Nucl. Part. Phys. **18**, 1419 (1992).
[10] S. Ohkubo and K. Yamashita, Phys. Lett. B **578**, 304 (2004).
[11] J. A. Maruhn, M. Kimura, S. Schramm, P.-G. Reinhard, H. Horiuchi, and A. Tohsaki, Phys. Rev. C **74**, 044311 (2006).
[12] T. Ichikawa, Y. Kanada-En'yo, and P. Möller, Phys. Rev. C **83**, 054319 (2011).
[13] J. Darai, J. Cseh, and D. G. Jenkins, Phys. Rev. C **86**, 064309 (2012).
[14] J. J. Kolata, R. A. Kryger, P. A. DeYoung, and F. W. Prosser, Phys. Rev. Lett. **61**, 1178 (1988).
[15] C. Beck, F. Haas, R. Freeman, B. Heusch, J. Coffin, G. Guillaume, F. Rami, and P. Wagner, Nucl. Phys. A **442**, 320 (1985).
[16] M. A. Eswaran, S. Kumar, E. T. Mirgule, D. R. Chakrabarty, V. M. Datar, N. L. Ragoowansi, and U. K. Pal, Phys. Rev. C **47**, 1418 (1993).
[17] D. G. Jenkins, C. J. Lister, M. P. Carpenter, P. Chowdury, N. J. Hammond, R. V. F. Janssens, T. L. Khoo, T. Lauritsen, D. Seweryniak, T. Davinson, P. J. Woods, A. Jokinen, H. Penttila, F. Haas, and S. Courtin, Phys. Rev. C **86**, 064308 (2012).
[18] J. Maas, E. Somorjai, H. Graber, C. Van Den Wijngaart, C. Van Der Leun, and P. Endt, Nucl. Phys. A **301**, 213 (1978).
[19] J. Cseh, E. Koltay, Z. Máté, E. Somorjai, and L. Zolnai, Nucl. Phys. A **385**, 43 (1982).
[20] T. Tanabe, K. Haga, M. Yasue, K. Sato, K. Ogino, Y. Kadota, M. Tochi, K. Makino, T. Kitahara, and T. Shiba, Nucl. Phys. A **399**, 241 (1983).
[21] S. Kubono, K. Morita, M. Tanaka, A. Sakaguchi, M. Sugitani, and S. Kato, Nucl. Phys. A **457**, 461 (1986).
[22] K. P. Artemov, M. S. Golovkov, V. Z. Goldberg, V. I. Dukhanov, I. B. Mazurov, V. V. Pankratov, V. V. Paramonov, V. P. Rudakov, I. N. Serikov, V. A. Solovev, and V. A. Timofeev, Sov. J. Nucl. Phys. **51**, 777 (1990).
[23] R. Stokstad, D. Shapira, L. Chua, P. Parker, M. W. Sachs, R. Wieland, and D. A. Bromley, Phys. Rev. Lett. **28**, 1523 (1972).

[24] H. Fröhlich, P. Dück, W. Galster, W. Treu, H. Voit, H. Witt, W. Kühn, and S. Lee, Phys. Lett. B **64**, 408 (1976).
[25] P. Charles, F. Auger, I. Badawy, B. Berthier, M. Dost, J. Gastebois, B. Fernandez, S. Lee, and E. Plagnol, Phys. Lett. B **62**, 289 (1976).
[26] D. James, G. Morgan, N. Fletcher, and M. Greenfield, Nucl. Phys. A **274**, 177 (1976).
[27] M. Shawcross, N. Curtis, W. N. Catford, N. M. Clarke, B. R. Fulton, S. J. Hall, J. T. Murgatroyd, S. P. G. Chappell, R. L. Cowin, G. Dillon, and D. L. Watson, Phys. Rev. C **63**, 034311 (2001).
[28] N. I. Ashwood, J. T. Murgatroyd, N. M. Clarke, M. Freer, B. R. Fulton, A. St. J. Murphy, S. P. G. Chappell, R. L. Cowin, G. K. Dillon, D. L. Watson, W. N. Catford, N. Curtis, M. Shawcross, and V. Pucknell, Phys. Rev. C **63**, 034315 (2001).
[29] D. Baye, Nucl. Phys. A **272**, 445 (1976).
[30] D. Baye and P.-H. Heenen, Nucl. Phys. A **283**, 176 (1977).
[31] K. Kato, S. Okabe, and Y. Abe, Prog. Theor. Phys. **74**, 1053 (1985).
[32] Y. Kondo and M. Katsuma, Nucl. Phys. A **738**, 226 (2004).
[33] J. Cseh, Phys. Rev. C **27**, 2991 (1983).
[34] P. O. Hess, A. Algora, J. Cseh, and J. P. Draayer, Phys. Rev. C **70**, 051303 (2004).
[35] H. Horiuchi and K. Ikeda, Prog. Theor. Phys. **40**, 277 (1968).
[36] Y. Suzuki, Nucl. Phys. A **470**, 119 (1987).
[37] T. Kawabata, H. Akimune, H. Fujita, Y. Fujita, M. Fujiwara, K. Hara, K. Hatanaka, M. Itoh, Y. Kanada-En'yo, S. Kishi, K. Nakanishi, H. Sakaguchi, Y. Shimbara, A. Tamii, S. Terashima, M. Uchida, T. Wakasa, Y. Yasuda, H. Yoshida, and M. Yosoi, Phys. Lett. B **646**, 6 (2007).
[38] Y. Kanada-En'yo, Phys. Rev. C **75**, 024302 (2007).
[39] T. Yamada, Y. Funaki, H. Horiuchi, K. Ikeda, and A. Tohsaki, Prog. Theor. Phys. **120**, 1139 (2008).
[40] H. Horiuchi, K. Ikeda, and K. Kato, Prog. Theor. Phys. Suppl. **192**, 1 (2012).
[41] Y. Chiba and M. Kimura, Phys. Rev. C **91**, 061302 (2015).
[42] Y. Chiba, M. Kimura, and Y. Taniguchi, Phys. Rev. C **93**, 034319 (2016).
[43] J. P. Elliott, Proc. R. Soc. London A **245**, 128 (1958).
[44] J. P. Elliott, Proc. R. Soc. London A **245**, 562 (1958).
[45] Y. Kanada-En'yo, M. Kimura, and H. Horiuchi, C. R. Phys. **4**, 497 (2003).
[46] Y. Kanada-En'yo and M. Kimura, in *Clusters in Nuclei*, edited by C. Beck, Lecture Notes in Physics Vol. 818 (Springer, Berlin, 2010), pp. 129–164.
[47] Y. Kanada-En'yo, M. Kimura, and A. Ono, Prog. Theor. Exp. Phys. **2012**, 1A202 (2012).
[48] J. Berger, M. Girod, and D. Gogny, Comput. Phys. Commun. **63**, 365 (1991).
[49] M. Kimura, R. Yoshida, and M. Isaka, Prog. Theor. Phys. **127**, 287 (2012).
[50] Y. Taniguchi, M. Kimura, and H. Horiuchi, Prog. Theor. Phys. **112**, 475 (2004).
[51] Y. Taniguchi, M. Kimura, Y. Kanada-En'yo, and H. Horiuchi, Phys. Rev. C **76**, 044317 (2007).
[52] Y. Taniguchi, Prog. Theor. Exp. Phys. **2014**, 73D01 (2014).
[53] D. L. Hill and J. A. Wheeler, Phys. Rev. **89**, 1102 (1953).
[54] J. J. Griffin and J. A. Wheeler, Phys. Rev. **108**, 311 (1957).
[55] J. K. Perring and T. H. R. Skyrme, Proc. Phys. Soc. London, Sect. A **69**, 600 (1956).
[56] B. Bayman and A. Bohr, Nucl. Phys. **9**, 596 (1958).
[57] T. Peach, U. Garg, Y. K. Gupta, J. Hoffman, J. T. Matta, D. Patel, P. V. M. Rao, K. Yoshida, M. Itoh, M. Fujiwara, K. Hara, H. Hashimoto, K. Nakanishi, M. Yosoi, H. Sakaguchi, S. Terashima, S. Kishi, T. Murakami, M. Uchida, Y. Yasuda, H. Akimune, T. Kawabata, M. N. Harakeh, and G. Colò, Phys. Rev. C **93**, 064325 (2016).
[58] P. Adsley, D. G. Jenkins, J. Cseh, S. S. Dimitriova, J. W. Brümmer, K. C. W. Li, D. J. Marín-Lámbarri, K. Lukyanov, N. Y. Kheswa, R. Neveling, P. Papka, L. Pellegri, V. Pesudo, L. C. Pool, G. Riczu, F. D. Smit, J. J. van Zyl, and E. Zemlyanaya, Phys. Rev. C **95**, 024319 (2017).